4D porosity evolution during pressure-solution of NaCl in the presence of phyllosilicates

4D porosity evolution during pressure-solution of NaCl in the presence of phyllosilicates

Alice Macente[a,1], Florian Fusseis[a], Ian B. Butler[a], Erika Tudisco[b], Stephen A. Hall[c], Edward Andò[d]

[a] University of Edinburgh, School of Geosciences, The King's Buildings, James Hutton Road, Edinburgh EH9 3FE

[b] Lund University, Division of Geotechnical Engineering, John Ericssons väg 1, Lund, Sweden

[c] Lund University, Department of Solid Mechanics, Ole Römers väg 1, 223 63 Lund, Sweden

[d] Univ. Grenoble Alpes, CNRS, Grenoble INP[2], 3SR, F-38000 Grenoble, France

Corresponding author: Alice Macente

Corresponding author's email: alice.macente@gmail.com

[1] Stanford University, Department of Geophysics, 397 Panama Mall, Stanford, CA 94305

[2] Institute of Engineering Univ. Grenoble Alpes

Abstract

Pressure-solution creep is one of the most common crustal deformation mechanisms, inducing changes in the porosity and permeability of rocks. For a variety of rock types undergoing pressure solution, it has been shown that the presence of phyllosilicates may significantly enhance the rate of the pressure-solution process. In this experimental investigation, we present 4-dimensional (three dimensions + time) X-ray microtomographic data that contrast deformation by pressure-solution of a pure NaCl aggregate with that of a mixture of NaCl and biotite. The results show that for mixed samples (NaCl+biotite), phyllosilicates induce a marked reduction in porosity and pore connectivity and contribute to an increase in the local strain rates by an order of magnitude over pure NaCl samples. At the same time, phyllosilicates do not induce strain localization in the sample. We discuss various possible explanations for these observations including a possible positive feedback between the porosity distribution and pressure solution. Our study yields novel insights into the local effects of phyllosilicates during pressure-solution creep and provides full 4-dimensional imaging and characterization of the coupled evolution of porosity and pore connectivity over previously unprecedented experimental time scales.

Keywords (6): pressure-solution creep; phyllosilicates; X-ray microtomography; Digital Volume Correlation; geochemical self-organization;

1. INTRODUCTION

Pressure-solution creep (PSC) is one of the key mechanisms of fluid-rock interaction and can induce significant changes in the transport properties and the composition of rocks. A wide range of geoscience applications, including hydrocarbon extraction, CO_2 storage and geothermal energy harvesting from hot sedimentary aquifers, rely on an accurate knowledge of the porosity and permeability of reservoir rocks. Understanding how these properties are affected by PSC is therefore of crucial importance.

PSC is a solution mass transfer process in response to the application of non-hydrostatic stresses that involves (i) dissolution at stressed contact points, (ii) mass transport through a fluid phase along grain boundaries, and (iii) re-precipitation of the dissolved material in the nearby low-stress areas (pores, veins) (Gratier et al., 2013; Rutter, 1983). PSC induces changes in the microstructure, pore structure, composition and strength of a wide range of geological materials (e.g. Aharonov and Katsman, 2009; Angevine and Turcotte, 1983; Bos et al., 2000; Croizé et al., 2010; Gratier, 1993; Gratier et al., 2005; Hickman and Evans, 1995, 1991; Lehner and Leroy, 2004; Pluymakers and Spiers, 2015). These alterations may, in turn, affect the transport properties of rocks (Sprunt and Nur, 1977, 1976). PSC has also been observed to trigger strain localization leading to the formation of stylolites (Gratier, 2003; Gratier et al., 2013;). Strain localisation during PSC has been recognized as involving feedbacks between solution/precipitation reactions and an evolving pore structure and thus a coupling between chemical, mechanical and hydraulic processes (Merino et al., 1983; Ortoleva et al., 1987).

While the effects of PSC on transport properties have been investigated extensively in a wide range of rocks (see Gratier et al. (2013), and references therein), the dynamic evolution of

these coupled processes at the grain scale remains poorly understood. This is primarily caused by the previously limited possibilities to image PSC in three dimensions over time. Renard et al. (2004) were the first to use 4-dimensional (4D, three spatial dimensions and time) synchrotron-based X-ray microtomography (μCT) to study the effects of PSC during compaction of pure NaCl aggregates. They imaged the reduced pore space and the impingement of grain contacts and inferred that the mean permeability in their samples decreased dramatically during compaction. Despite its pioneering character, this study did not explore PSC in the presence of phyllosilicates, which have been shown to hold the potential to significantly affect the rate of PSC (Aharonov and Katsman, 2009; Bos and Spiers, 2002; Hickman and Evans, 1995; Renard et al., 1997). Here we present 4D X-ray microtomographic data that contrast the deformation of a pure NaCl aggregate by PSC with that of a mixture of NaCl and biotite, in order to investigate the effects of phyllosilicates on the progressive shortening and the concomitant evolution of porosity and pore connectivity of the samples. The combination of μCT with *Digital Volume Correlation* (DVC, e.g. Andò et al., 2012; Tudisco et al., 2017) enables quantification of strain and strain rates at the grain scale and following of the evolution of these parameters during sample compaction. Our findings suggest that in NaCl aggregates: i) bulk porosity and pore connectivity are critically reduced in the presence of phyllosilicates; ii) phyllosilicates contribute to increase the strain rates achieved by PSC by an order of magnitude with respect to the monomineralic NaCl domains.

2. MATERIAL AND METHODS

2.1 Introduction

77 We use NaCl aggregates as analogues for geomaterials and sedimentary rocks undergoing
78 PSC. Previous compaction experiments have demonstrated that NaCl samples deform
79 sufficiently quickly to enable the study of PSC in a laboratory environment at room temperature
80 (Gratier, 1993; Renard et al., 2004, 2001; Schutjens and Spiers, 1999; Spiers et al., 1990).

81 **2.2 Materials**

82 **2.2.1 Sample Preparation**

83 Two different samples were prepared in x-ray transparent uniaxial presses (see section
84 2.2.2) to test the effect of different sample compositions on PSC. The total sample mass was
85 chosen to produce cylindrical samples with diameters of 5 mm and an initial height of ~5 mm.
86 For the first sample, granular NaCl (analytical reagent, Fisher Scientific) was sieved to a 250-300
87 µm grain size. This sample acted as our monomineralic reference. The second sample consisted
88 of a mixture of NaCl and biotite grains at a ratio, by mass, of 4:1. The NaCl was sieved to give
89 the same grain size as the first sample. Biotite flakes with grain sizes between 212 and 750 µm
90 (longest dimension) were obtained by cutting mica sheets from a biotite single crystal using a
91 scalpel. Biotite was chosen because of the contrast in X-ray absorption with respect to NaCl; in
92 µCT data biotite flakes appears as bright grains, NaCl appears as light grey grains, while (brine-
93 filled) pores are dark grey (Fig. 1). In the press, the NaCl/biotite mixture (1.4 mm thick) was
94 confined by two pure NaCl layers (0.95 mm top layer, 1.27 mm bottom layer). In this way, the
95 two pure NaCl layers constitute a 'reference' material within the sample to compare the degree
96 of compaction under the same experimental conditions. The materials were introduced into the
97 presses sequentially as slurries. Biotite within the central layer showed no preferential
98 alignment prior to compaction. In each of the two samples, two discs of filter paper were

placed above and below of the samples, to avoid grains clogging the fluid connections. Both samples were saturated with NaCl solution. The initial porosity of the two sample compositions has been calculated from the mass of the salt quantitatively added and the dimensions of the initial salt reference stack. The pure NaCl sample exhibits an initial porosity of ~36%, while the sample with biotite, due to the different grain packing and an initial different height (5 mm in NaCl vs 3.7 mm in NaCl-biotite), exhibits a porosity of ~33%.

2.2.2. Experimental Setup

The samples were compacted in X-ray transparent presses. These experimental presses were built in-house and comprise a 5 mm diameter cylindrical piston that was fashioned to be a close running-fit to the lower cylindrical sample chamber (Supplementary Fig. S3). The cells were manufactured from PEEK (Polyether-ether-ketone). Loading frames, composed of two 20 mm thick Perspex plates joined by three threaded rods, allowed a pneumatic actuator to apply a constant uniaxial load on the samples. The close running-fit of the piston enabled a narrow annulus of high-vacuum silicone grease to be used to provide a fluid seal between the piston and sample chamber.

Initial loading of the sample using the pneumatic actuator for 10 minutes was used to produce a pre-compacted starting material. At this stage, a reference μCT scan was acquired (see section 2.2.3). Subsequently, the inlet and outlet tubes to the cell, as well as the sample, were flushed with a pre - saturated NaCl solution to ensure that no air bubbles remained in the system, enabling the experiments to start saturated with brine. To maintain fluid saturation, a pre-saturated NaCl solution filled reservoir attached to the lower fluid inlet of the cell was

mounted ~40 cm above the cells (Supplementary Fig. S3). The sample was then loaded to a constant uniaxial stress which was stable between 6.4 and 6.6 MPa.

2.2.3 Image Acquisition

During each experiment, 3D µCT data were acquired using the custom-built microtomograph in the School of Geosciences, at the University of Edinburgh (see Cnudde and Boone (2013), for the fundamentals of laboratory X-ray µCT and Table S1 for data acquisition parameters). Combined, the data acquired during the experiments formed a 3D time series, i.e. 4D datasets. Compaction was interrupted for scanning of the samples. For each sample, twelve µCT datasets were acquired over 2455 hours of compaction (Fig. 2, 3, Table S2), allowing monitoring of the evolution of porosity and grain morphologies over time. Initially, the samples were scanned in short time intervals (2, 4, 6 hours), to monitor the mechanical behaviour of the samples, and capture relatively rapid initial deformation. Successively, the time interval between each scan was increased to monitor the progressively slower deformation of the sample (Table S2).

2.2.4 Image Processing

The µCT data were reconstructed using Octopus® software (Dierick et al., 2004) yielding a voxel (3-dimensional pixel) volume of 6.5^3 μm^3. The twelve microtomographic volumes acquired for each deformation experiment were analysed individually, to assess sample compaction and to measure the evolution of porosity and pore connectivity. The height of the samples in between the top piston and the bottom of the cell was measured from the vertical slices through each µCT scan, and the relative shortening was calculated through

$$\varepsilon_t = \frac{x_0 - x_t}{x_0}$$

where x_0 represents the initial height of the sample (measured from the reference scans), and x_t represents the height at a given time *t*. The µCT datasets were denoised using a *median filter* with a kernel size 2. Subvolumes of dimensions 400^3 voxels, equivalent to a cube of 17.6 mm^3 (i.e., 2.6 mm on each side), were cropped from the central regions of the reconstructed µCT volumes to conduct porosity analyses and avoid artefacts from the cell boundaries. The workflow, applied in AvizoFire® v. 8 and Avizo® v. 9, is detailed in Supplementary Figure S4. The pore space was segmented by the application of an *interactive threshold* to produce binarised image stacks from which the total porosity was determined using the *volume fraction* operator (Arns et al., 2002) (Fig. 4a). The sensitivity of the segmentation and interconnectivity analysis to changes in the threshold values was established by repeating the procedure on volumes that were eroded and dilated by one voxel (see Fusseis et al. (2012) and Macente et al. (2017) for details of the analysis). This procedure yielded error bars on the porosity measurements. Slice-by-slice (2-dimensional) porosity analyses were also performed to determine the evolution of the porosity along the direction of loading (Fig. 4b, c, d).

Pore space connectivity was characterized in the segmented data using the *label* function and a voxel coordination value of six, where the *labeling* operator identifies neighbouring voxels that share a cube face and assigns them to an individual pore cluster (Fig. 5, 6). From these clusters, individual pores were separated using the *Separate Objects* operator with a coordination number of six, and a marker extent equal to one (least connected objects). Separation points represent pore throats. Subsequently, the individual pores were analysed for their volume in the individual datasets using the *Label analysis* operator. The smallest pores considered in the pore size distribution analyses were 10 voxels in volume, or 2.7 x 10^3 μm^3.

We treated the central mixed layer and the marginal pure NaCl layers in the NaCl-biotite sample as three discrete subdomains in order to assess and compare their relative evolution. From the 400^3 voxels subvolumes, these subdomains were extracted using the *Extract volume* operator in Avizo, by identifying where the biotite flakes first occur and end vertically along the sample. The marginal NaCl layers were also compared with the pure NaCl sample.

2.3 Digital Volume Correlation (DVC)

Digital Volume Correlation (DVC) was used to measure the local distribution of displacements (from which maximum shear strains and volumetric strains are obtained) in the sample between two successive time steps (see Supplementary Material for details on the technique). DVC, which spatially resolves displacements with a sub-voxel accuracy, was performed on consecutive pairs of µCT 3D datasets using the code *TomoWarp2 (Tudisco et al., 2017)* and computed on the Edinburgh Compute and Data Facility's Terracorrelator cluster (Atkinson et al., 2015). Results were visualized in the open-source software Fiji (Schindelin et al., 2012). Misalignments in x and y, and misorientation in excess of 5° between the two 3D datasets can introduce errors in the outputs of the correlation and needed to be corrected. Two small markers at the base of the experimental cells were used together with the central fluid bore in the press to define the position and orientation of the datasets to enable the correction of misalignments and misorientations between two subsequently acquired time steps using the *rotate* and *translate* operators in Fiji. Figures 7 and 8 show the 3-dimensional results of DVC represented by XZ vertical slices through the middle of the analysis volumes for progressively shortened datasets. Absolute strain-rate values were calculated by dividing the DVC strains by the duration of loading (in seconds) between each analysed µCT scan (Fig. 9).

2.4 Scanning electron microscopy

Secondary electron images were acquired after the deformation experiments to study the grain-scale effects of pressure solution in the sample. Before retrieving the samples, the brine was displaced using compressed air. The samples were then retrieved from the uniaxial cells and portions of the samples carefully extracted. This procedure may introduce physical damage to the sample microstructures. For this reason, we only investigated evidence for PSC (i.e. indented grains, suture zones) in areas that were 'undisturbed' and represented consolidated portions of the original samples. Gold coated samples were imaged using a Carl Zeiss SIGMA HD VP Field Emission SEM with an acceleration voltage of 10 kV. Samples were mounted on an aluminium stub using a self-adhesive conducting pad prior to gold coating.

3. RESULTS

3.1 Bulk deformation

The measurements of vertical shortening show that the *pure NaCl* sample shortened a total of 25 % over 2455 hours of compaction. The compaction curve was initially steep, where the sample accommodated 10 % vertical shortening in 22.5 hours. Between 155 and 255 hours, the compaction rate slowed down. Beyond 400 hours of compaction, the gradient of the curve did not change substantially and we consider the sample to deform in steady state there (Fig. 2a). The compaction curve for the *NaCl-biotite* sample displays an identical pattern. However, the sample reached a total of 35 % vertical shortening at the end of the experiment, with very fast shortening of ~17 % in the first 22.5 hours. Compaction decelerated over the same time interval as the pure NaCl sample, again reaching what appears to be a steady state deformation. In both experiments, compaction was still ongoing at the end of the experiment.

These trends are reflected by the evolution of bulk strain rates over time (Fig. 2b). The data showed an immediate decrease in bulk strain rates after initial compaction. Some differences were present between 208 and 376 hours of compaction, when the two samples deformed less over a significant time period, resulting in lower strain rates (Fig. 2b).

Inspection of vertically centred slices through the μCT data revealed some key differences between the two samples (Fig. 3). The NaCl sample showed no microstructures indicative of the action of cataclasis, nor indented grains to have formed in the first 100 hours. However, after some compaction, porosity was reduced and grains started to agglomerate (Fig. 3c, d). In the NaCl-biotite sample, the porosity reduction was localised in the biotite-bearing layer early on (Fig. 3f). In this layer, NaCl grains lost their cubic habit with increasing compaction. Biotite generally showed a progressive alignment in the direction perpendicular to the loading, although some grains were trapped in their orientation and left without room to move (Fig. 3 e-h, centre bottom). In comparison, the marginal NaCl layers developed fewer NaCl grain impingements, and ~10 % of porosity remained after 2455 hours of compaction. These observations mirrored those from the pure NaCl sample.

3.2 Porosity evolution

3.2.1 Bulk Porosity

We analyzed the distribution of porosity change during compaction in the cropped subvolumes to identify any heterogeneities that could be indicative of strain localization in our samples and to evaluate the evolving transport properties (Fig. 4a). In the case of the pure NaCl sample, as compaction proceeded the bulk porosity was reduced from 36 to ~13 % (Fig. 4a).

Slice-by-slice porosity measurements along the vertical axis of the sample (Z-direction) confirm that this porosity reduction was evenly distributed in the sample and that no strain localization had taken place (Fig. 4b, c, d). The upper portion of the sample showed a slightly larger decrease in porosity as compared to the rest of the sample. In the case of NaCl-biotite sample, bulk porosity decreased by ~25 % over the duration of the experiment (Fig. 4a). The slice-by-slice analysis shows that at some vertical positions porosity decreased to 0 % after 2465 hours of compaction (Fig. 4d).

To better illustrate the effect of sample composition, shortening was evaluated separately for the biotite-bearing layer and the marginal NaCl layers of this sample (Fig. 5). The marginal NaCl-bearing layers were combined in the analysis. Essentially, shortening was accommodated to roughly equal parts by all three layers. The biotite-bearing layer shortened marginally more (36 %), with its thickness decreasing from 1.4 mm to 0.9 mm over 2455 hours (Fig. 5). In the same time interval, the NaCl layers shorten from 2.2 mm to 1.5 mm in total (35 % shortening). This analysis also reveals how shortening was partitioned between the three layers (Fig. 5). Initially, both layers compacted at about the same rate. At 91 hours, the shortening was partitioned into the marginal NaCl layers, a development that continued to 376 hours. At 137.5 hours the pore connectivity in the biotite-bearing layer broke down (see section 3.2.2 below), as shown by the grey shaded area in Fig. 5. This event was followed by accelerated compaction in the biotite-bearing layer and a deceleration of compaction in the NaCl layers. From 376 hours onwards, both layers compacted at about the same rate, until the end of the experiment.

We further analysed the pore size distribution in the two sample compositions (Supplementary Fig. S5) for three compaction steps (beginning, middle and end of the compaction). In both samples, the absolute frequency of larger volume pores decreased and that of smaller pores increased with increasing compaction. In the NaCl sample, small pores (volume < 2.6 x 10^5 μm^3) doubled in frequency with increasing deformation. However, these pores contributed relatively small amounts to the total pore volume (Supplementary Fig. S5c). Similar observations were made in the NaCl-biotite sample. To better understand the effect of the central biotite-bearing layer, we analysed the pore size distributions in this layer and the marginal NaCl layers in five increasingly shortened datasets (Supplementary Fig. S6). The pore size distribution for the marginal NaCl layers showed a general increase in smaller pore sizes (volumes < 2.6 x 10^5 μm^3) and a corresponding decrease in the number of larger pores, which resembled the evolution of the pure NaCl sample (Supplementary Fig. S6a). However, the central biotite-bearing layer showed a much more marked reduction for large pores (Supplementary Fig. S6b).

3.2.2. Pore Connectivity

We further analysed how compaction affected pore connectivity via pore throats (as opposed to grain boundaries, which we could not resolve in our data) in the two samples. The homogeneity of the pure NaCl sample is assumed to be responsible for the preservation of a percolating pore network throughout the sample until the end of the experiment (Fig. 6). The largest connected pore cluster (volume > 2.7 x 10^8 μm^3) initially accounted for all the pore space; however, in later compaction stages ~3 % of the porosity was accommodated by

smaller, isolated pores (Fig. 6 top). In contrast, the NaCl-biotite sample was characterized by a marked difference in the evolution of pore connectivity in the central NaCl-biotite layer and the marginal NaCl layers (Fig. 6 bottom). While the pore space was initially connected throughout the entire sample, with 99.8 % of the segmented porosity being accommodated by a single pore cluster, porosity started to disconnect vertically across the NaCl-biotite layer after 137.5 hours of compaction. Eventually two large pore clusters, disconnected from each other, remained present at the top and bottom of the sample, in total constituting 88 % of the total pore space (Fig. 6). A significant proportion of porosity was accommodated by smaller, isolated pores, mostly located at the interfaces with the marginal NaCl layers (not shown in Fig. 6).

3.3 Local strains and strain rates: results from DVC analysis

DVC was applied to every successive pair of compaction steps, yielding the evolving displacement fields during the entire experiment using eleven DVC datasets per sample. The DVC analysis of the pure NaCl sample showed a relatively homogeneous distribution of shear strains, with local maxima (Fig. 7, Supplementary Gif1). These zones correspond to zones where the volumetric strain is negative, indicating compaction (white circles in Fig. 7).

In comparison, the DVC analysis of the NaCl-biotite sample showed a much more heterogeneous shear strain distribution at the beginning and again at the end of the experiment, with a concentration of shear strains in the NaCl-biotite layer (Fig. 8, Supplementary Gif2). The analyses of volumetric strains in this sample showed a concentration of compaction in the centre of the sample (white circles in Fig. 8), with the highest strains being accumulated in the early and late stages of the experiment.

Calculating the local integrated strain rates from DVC analyses enabled contrasting the bulk compaction rate of each sample with locally resolved strain rates on the grain scale (Fig. 9). While in both samples the bulk compaction rates decreased by two orders of magnitude during the duration of the experiment (10^{-6} to 10^{-8} s^{-1}, Fig.2), locally (i.e. on the grain scale) both samples showed significant deviations in strain rates (Fig. 2). In the pure NaCl sample, the local shear strain rates decreased from 10^{-6} – 10^{-7} to 10^{-8} – 10^{-9} s^{-1}, whereas volumetric strain rates decreased from -10^{-6} to -10^{-8} s^{-1} in the most compacted areas. However, these values were evenly distributed within the sample (Fig. 9). In contrast, the shear strain rates reached maximum values of 10^{-7} s^{-1} in the presence of biotite, while the highest volumetric compaction rates were -6×10^{-8} s^{-1}. The high shear- and lower volumetric strain rates occur in the central NaCl-biotite layers (Fig. 9) and are an order of magnitude higher than in the rest of the sample.

3.4 Microstructural evidence for PSC

SEM images of the recovered samples were acquired in order to verify the microstructural changes and to collect evidence for PSC, if present, on the grain scale (Fig. 10). Indented contacts would provide evidence for PSC consistent with that proposed by Passchier and Trouw (2005) (page 31, box 3.2). In the pure NaCl sample, grains that have lost their original cubic habits are clearly visible (Fig. 10a, b). In some areas, it is possible to recognize triple junctions (Fig. 10a) and suture zones between grain interfaces, where the two grain contacts are highly indented (Fig. 10b). In the presence of phyllosilicates, indentations are obvious and NaCl grains can be seen that have dissolved against (less soluble) biotite grains, and NaCl grains that have lost their cubic habit and have become more rounded are also

315 evident (Fig. 10c, d). In the pure NaCl portions of this sample, indentations between NaCl grains
316 can still be observed, but the grains have retained more of their original habit (Fig. 3).

317 **4. DISCUSSION**

318 **4.1 Bulk and local deformation evolution**

319 Our experiments enable a direct comparison of bulk compaction behaviour with local
320 grain-scale responses and thus allow novel insights into the effects of sample composition on
321 the deformation processes. The bulk compaction curves of the two investigated sample
322 configurations (Fig. 2a) show a strong non-linear decrease in the compaction rate over time,
323 which is in agreement with findings from previous studies and support our conclusion that NaCl
324 deforms by PSC (Hickman and Evans, 1995, 1991; Renard et al., 2004; Schutjens and Spiers,
325 1999; Spiers et al., 1990). However, the duration of our experiments considerably exceeded
326 that of many published studies (Renard et al., 2004; Rutter and Wanten, 2000; Spiers et al.,
327 1990;), which allows a more detailed assessment of the evolution of compaction behaviour of
328 halite samples. Earlier, shorter studies by Renard et al. (2004) and Spiers et al. (1990) showed a
329 very similar compaction behaviour despite slightly different experimental setups. Renard et al.
330 (2004) used a smaller grain size of sieved NaCl (100-150 µm), and smaller loads (0.1 to 0.6 MPa)
331 and conducted their experiment at room temperature for seven days. The compaction rate
332 decreased over time, showing an initial steep gradient, as in our data, and reaching 18 % of
333 vertical shortening after three days. They concluded that the presence of clays supports grain
334 contact healing, reducing porosity and favouring pressure-solution creep. Spiers et al. (1990)
335 performed tests on brine-saturated NaCl powder (grain size 100-275 µm) at temperatures of
336 20-90°C and applied stresses of 0.5-2.2 MPa, testing theoretically-derived constitutive

337 equations. Their grain sizes and time intervals are similar to ours, and their results showed
338 similar orders of bulk strain rates. The data presented here explore the time evolution beyond
339 the initial steep compaction rate shown in these studies and provide a visual assessment of the
340 micro-scale processes, feeding into a better understanding of the role of phyllosilicates.

341 The striking observation from our own experiments is that both samples follow
342 essentially the same bulk compaction path, with a very rapid initial compaction characterized
343 by variable rates (Fig. 2 a, b), replaced by what appears to be steady state compaction after
344 about 400 hours. We interpret mechanical grain rearrangements and accelerated dissolution
345 rates at initially relatively small and, therefore, highly stressed grain contact areas to be
346 responsible for the high compaction rates during the early stages of the experiments. The
347 decrease in the compaction rate up to about 400 hours might broadly reflect an increase in
348 grain contact area and the associated decrease in local normal stresses as drivers for
349 dissolution.

350 From about 400 hours until the end of the experiments at 2455 hours, both experiments
351 compacted by PSC at virtually the same constant rates (Fig. 2b), which raises questions about
352 the actual effect of biotite upon PSC in the NaCl-biotite sample. In our interpretation, we
353 consider it of importance that, while the local shear strain rates reached up to 3×10^{-8} s^{-1} in the
354 pure NaCl sample, these maxima tended to be transient in terms of their location and moved
355 throughout the sample (cf. Fig. 9a). We interpret this as the capture of dynamic
356 rearrangements of stresses in the compacting sample (see below). The NaCl-biotite sample
357 showed similar magnitudes of local strain rates, but in that case, these were clearly associated
358 with the loci of biotite flakes and remained so over the entire duration of the experiment (Fig.

359 8, 9). We further observe that the presence of biotite was clearly related to the reduction of
360 porosity (Fig. 4 b-d), which, in the absence of strain localization in the central NaCl-biotite layer
361 (Fig. 5), cannot be ascribed to pore collapse there and rather points to pores having been filled.
362
363 On the basis of these observations, we interpret PSC in the NaCl and NaCl-biotite layers,
364 to have operated under different conditions in the two layers. We envisage the overall load in
365 pure granular NaCl samples, at least initially, to have been distributed over “force chains”. The
366 concept of force chains in compacting granular materials considers the overall load to be
367 distributed heterogeneously among the grains, with a minority of grains that carry above-
368 average loads forming a strong load-bearing framework, while the majority of grains constitute
369 a weak granular aggregate (e.g. Peters et al., 2005). In our conceptual model, a force chain will
370 localize pressure solution in a granular NaCl aggregate along an axis that is broadly aligned with
371 the bulk shortening direction and over an initially small grain contact area. The idea of *dynamic*
372 *force chains* entails that the lifetime of a particular force chain is limited by the dynamic
373 redistribution of loads within the granular aggregate as locally increased normal stresses lead to
374 enhanced PSC and accelerated shortening, and a relative increase of the grain surface area
375 along the force chain. When loads are redistributed, the load-bearing framework changes its
376 geometry. Our DVC analysis indicates that the strain within the pure NaCl sample varies in
377 space and time; we interpret this to indicate a rearrangement of stresses and the emergence of
378 new dynamic force chains in the pure NaCl layers.
379 While, in principal, the conceptual model described above may also apply to the NaCl-
380 biotite layer, our DVC analysis indicates that compaction there was tied to the biotite grains and

381 we interpret PSC to have been accelerated by the higher chemical potential associated with
382 phase boundaries (Aharonov and Katsman, 2009; Hickman and Evans, 1995). Factors such as
383 particle shape, particle size, and contact area may also have played a significant role in
384 controlling the evolution of PSC. Meyer et al. (2006) and Van den Ende et al.(2018)
385 demonstrated how particle shapes and the shape of the contact between the particles
386 influence compaction rates in pressure-solution. Pluymakers and Spiers (2015) emphasized the
387 significance of the nature of the contact surfaces where irregularities lead to faster dissolution.
388 The initial geometric arrangement of the grain contacts between a cube and a plate-like mineral
389 (i.e. salt vs biotite) may create 'asperities', with lower contact areas, which could have assisted
390 the driving force of the mechanism. From 400 hours onward, the process might have slowed
391 down because reduced porosity was met by reduced asperities/irregularities in the grains,
392 which became progressively smoother as compaction progressed (lower contact stresses). We
393 envisage that these mechanisms contributed to pressure solution. Whichever the reason, the
394 local strain rate data from our DVC analysis suggest that this enhanced PSC drove the initial
395 compaction in the NaCl-biotite layer (Fig. 9). However, with increasing shortening, the contact
396 areas in the NaCl layer increased, which lowered the stresses at contact points and, as a
397 consequence reduced the driving force for PSC. DVC reveals that both the local volumetric and
398 the shear strain rates decreased by almost an order of magnitude in the NaCl-biotite layer
399 between 150 and 400 hours of compaction (Fig. 9, central column), which we consider to be
400 supporting evidence for this interpretation.

401 Compaction of the central NaCl-biotite layer was accompanied by a significant reduction
402 of the porosity, to such a degree that pore connectivity broke down across the central layer

403 early in the experiment (Fig. 3, 4 and 6). However, at the same time, this layer did not compact
404 significantly more than the surrounding NaCl layers (Fig. 5). It is generally assumed that the
405 transport distances during pressure solution of NaCl in a stagnant, saturated brine are on the
406 order of the grain size and material is re-precipitated in the nearby pore space (e.g. Gratier et
407 al., 2013; Gundersen et al., 2002; Weyl, 1959). For our experiments this would mean that the
408 porosity in the NaCl and NaCl-biotite layers should have decreased in proportion with the
409 compaction. Given that this was clearly not the case, porosity reduction in the NaCl-biotite layer
410 cannot have been accomplished by pore collapse during compaction. We speculate that the
411 disproportional decrease of porosity in the NaCl-biotite layer was caused by additional salt
412 being deposited there and, invoke Merino et al.'s model for a texture-pressure solution
413 coupling to explain this (Dewers and Ortoleva, 1988; Merino et al., 1983; Ortoleva et al., 1987).
414 Merino suggests that, in a positive feedback loop, dissolved material should diffuse towards
415 areas with a relatively lower porosity and, therefore, larger grain contact area and
416 correspondingly lower stresses. In our experiment, this would mean that material was
417 transported from the pure NaCl layers to the central NaCl-biotite layer. In the former, the
418 removal of dissolved material leaves less material to carry the load, which increases the driving
419 force for PSC. At the same time, loads are distributed over an increasingly larger area at the
420 deposition sites in the NaCl-biotite layer, which should slow down PSC there. We interpret our
421 quantitative observations to provide evidence that dissolved salt has indeed been transferred
422 from the marginal NaCl into the central NaCl-biotite domain. Once connectivity into the NaCl-
423 biotite was lost, the interface between the two domains would have become the locus for
424 enhanced deposition (Fig. 3).

425 **4.2 Implications for fluid flow and permeability in rocks deforming by PSC**

426 Our experiments provide new insights into the effects of PSC on the spatio-temporal
427 evolution of porosity and pore connectivity, which influence transport properties, and
428 consequently fluid flow. These effects have been intensively studied, particularly for the case of
429 stylolites. Stylolites commonly develop in carbonates, silicate rocks, sandstones and mudstones
430 (Benedicto and Schultz, 2010; Gratier et al., 2013; Heap et al., 2014; Park and Schot, 1968).
431 They can induce up to 50 % of dissolution in the host rock with important implication for solute
432 transport and fluid flow (Aharonov and Katsman, 2009). However, it remains unclear whether
433 stylolites act as barriers to fluid flow (Alsharhan and Sadd, 2010) or become fluid conduits
434 (Heap et al., 2014;). Our experiments, which were conducted under the reported, specific
435 boundary conditions, show that the disconnection of the pore space with increasing
436 deformation leads to a very efficient hydraulic compartmentalization of the sample. The
437 porosity evolution in the central layer would suppress any potential fluid flow across the layer
438 and constrain fluid movements to the NaCl layers, at least at the scale and resolution of our
439 data. At the same time, it would allow fluid that is trapped inside the NaCl-biotite layer to
440 equilibrate chemically with its local host, whereas fluid in the percolating NaCl layers would
441 form part of an open chemical system. Our results support the interpretation by Heap et al.
442 (2014) that stylolites may compartmentalize fluid flow, allowing movement in the marginal
443 layers and in the directions perpendicular to the shortening direction.
444
445 Our findings feed into an improved understanding of fluid transport properties in
446 hydrocarbon reservoirs where PSC is active (Ghanbarzadeh et al., 2015; Torabi et al., 2015).

Alsharhan and Sadd (2010) and Heap et al. (2014) show that stylolites are capable of reducing permeability when the rock is enriched in minerals such as phyllosilicates. The effect of biotite on the permeability of the halite rocks remains unclear and will be addressed using a modelling approach in a follow-up study.

5. CONCLUSIONS

We have analysed the first 4D microtomographic dataset that documents pressure solution creep in NaCl-biotite aggregates over several months. Our results indicate that phyllosilicates contribute to reduce bulk porosity and induce a significant decrease in pore connectivity, causing a hydraulic compartmentalization of the sample. The measured local strain rates indicate that phyllosilicates enhance the pressure-solution process by increasing the local strain rates. These results highlight the key role of phyllosilicates in affecting the rock microstructure under pressure-solution creep and provide new insights into the spatio-temporal evolution of transport properties.

ACKNOWLEDGEMENTS

The authors would like to thank Dr. Nicola Cayzer for help at the SEM and Robert Brown and Alex Hart for manufacturing the experimental cells and straining frames. All three are from the School of Geosciences, University of Edinburgh. We furthermore thank Dr. Anne Pluymakers and an anonymous reviewer for extremely encouraging and constructive reviews. The work was supported by the PhD studentship funding from the School of Geosciences, University of Edinburgh.

REFERENCES

Aharonov, E., Katsman, R., 2009. Interaction between pressure solution and clays in stylolite development: Insights from modeling. Am. J. Sci. 309, 607–632. https://doi.org/10.2475/07.2009.04

Alsharhan, A.S., Sadd, A.L., 2010. Stylolites in Lower Cretaceous Carbonate Reservoirs, U.A.E. Soc. Sediment. Geol. https://doi.org/10.2110/pec.00.69.0185

Andò, E., Bésuelle, P., Hall, S.A., Viggiani, G., Desrues, J., 2012. Experimental micromechanics: grain-scale observation of sand deformation. Géotechnique Lett. 2, 107–112. https://doi.org/10.1680/geolett.12.00027

Angevine, C.L., Turcotte, D.L., 1983. Porosity reduction by pressure solution: a theoretical model for quartz arenites. Geol Soc Amer Bull 94, 1129–1134. https://doi.org/10.1130/0016-7606(1983)94<1129

Arns, C.H., Knackstedt, M.A., Pinczewski, W. V., Garboczi, E.J., 2002. Computation of linear elastic properties from microtomographic images: Methodology and agreement between theory and experiment. Geophysics 67, 1396. https://doi.org/10.1190/1.1512785

Atkinson, M., Bell, A., Curtis, A., Entwistle, E., Filgueira, R., Main, I., Meles, G., Miniter, M., Zhao, Y., 2015. The Terracorrelator : a shared memory HPC facility for real-time seismological cross-correlation analyses. Geophys. Res. Abstr. Eur. Geosci. Union Gen. Assem. 17.

Benedicto, A., Schultz, R.A., 2010. Stylolites in limestone: Magnitude of contractional strain accommodated and scaling relationships. J. Struct. Geol. 32, 1250–1256. https://doi.org/10.1016/j.jsg.2009.04.020

Bos, B., Spiers, C.J., 2002. Frictional-viscous flow of phyllosilicate-bearing fault rock : Microphysical model and implications for crustal strength profiles. J. Geophys. Res. 107,

2028.

Cnudde, V., Boone, M.N., 2013. High-resolution X-ray computed tomography in geosciences: A review of the current technology and applications. Earth-Science Rev. 123, 1–17. https://doi.org/10.1016/j.earscirev.2013.04.003

Croizé, D., Bjørlykke, K., Jahren, J., Renard, F., 2010. Experimental mechanical and chemical compaction of carbonate sand. J. Geophys. Res. Solid Earth 115, 1–17. https://doi.org/10.1029/2010JB007697

Dewers, T., Ortoleva, P., 1988. The role of geochemical self-organization in the migration and trapping of hydrocarbons. Appl. Geochemistry 3, 287–316. https://doi.org/10.1016/0883-2927(88)90108-4

Dierick, M., Masschaele, B., Hoorebeke, L. Van, 2004. Octopus, a fast and user-friendly tomographic reconstruction package developed in LabView®. Meas. Sci. Technol. 15, 1366–1370. https://doi.org/10.1088/0957-0233/15/7/020

Fusseis, F., Schrank, C., Liu, J., Karrech, A., Llana-F??nez, S., Xiao, X., Regenauer-Lieb, K., 2012. Pore formation during dehydration of a polycrystalline gypsum sample observed and quantified in a time-series synchrotron X-ray micro-tomography experiment. Solid Earth 3, 71–86. https://doi.org/10.5194/se-3-71-2012

Ghanbarzadeh, S., Hesse, M.A., Prodanović, M., Gardner, J.E., 2015. Deformation-assisted fluid percolation in rock salt. Science (80-.). 350, 1069–1072. https://doi.org/10.1126/science.aac8747

Gratier, J.P., 2003. Modeling fluid transfer along California faults when integrating pressure solution crack sealing and compaction processes. J. Geophys. Res. 108, 1–25.

https://doi.org/10.1029/2001JB000380

Gratier, J.P., 1993. Experimental pressure solution of halite by an indenter technique. Geophys. Res. Lett. 20, 1647–1650.

Gratier, J.P., Dysthe, D.K., Renard, F., 2013. The role of pressure solution creep in the ductility of the Earth ' s upper crust, Advances in Geophysics. https://doi.org/10.1016/B978-0-12-380940-7.00002-0

Gratier, J.P., Muquet, L., Hassani, R., Renard, F., 2005. Experimental microstylolites in quartz and modeled application to natural stylolitic structures. J. Struct. Geol. 1–24.

Gundersen, E., Renard, F., Dysthe, D.K., Bjørlykke, K., Jamtveit, B., 2002. Coupling between pressure solution creep and diffusive mass transport in porous rocks. J. Geophys. Res. Solid Earth 107, ECV 19-1-ECV 19-19. https://doi.org/10.1029/2001JB000287

Heap, M.J., Baud, P., Reuschle, T., Meredith, P.G., 2014. Stylolites in limestones: Barriers to fluid flow? Geology 42, 51–54. https://doi.org/doi: 10.1130/G34900.1

Hickman, S.H., Evans, B., 1995. Kinetics of pressure solution at halite-silica interfaces and intergranular clay films. J. Geophys. Res. Earth 100, 13113–13132. https://doi.org/10.1029/95JB00911

Hickman, S.H., Evans, B., 1991. Experimental pressure solution in halite : the effect boundary structure of grain / interphase. J. Geol. Soc. London. 148, 549–560. https://doi.org/10.1144/gsjgs.148.3.0549

Lehner, F., Leroy, Y., 2004. Sandstone Compaction by Intergranular Pressure Solution. Guéguen, Y., Boutéca, M. (Eds.), Mech. Fluid-Saturated Rocks. Int. Geophys. Ser. Vol. 89, pp. 115–168 2004. 1–54.

534 Macente, A., Fusseis, F., Menegon, L., Xianghui, X., John, T., 2017. The strain-dependent spatial
535 evolution of garnet in a high-P ductile shear zone from the Western Gneiss Region
536 (Norway): a synchrotron X-ray microtomography study. J. Metamorph. Geol. 35, 565–583.
537 https://doi.org/10.1111/jmg.12245
538 Merino, E., Ortoleva, P., Strickholm, P., 1983. Generation of evenly-spaced pressure-solution
539 seams during (late) diagenesis: A kinetic theory. Contrib. to Mineral. Petrol. 82, 360–370.
540 https://doi.org/10.1007/BF00399713
541 Meyer, E.E., Greene, G.W., Alcantar, N.A., Israelachvili, J.N., Boles, J.R., 2006. Experimental
542 investigation of the dissolution of quartz by a muscovite mica surface: Implications for
543 pressure solution. J. Geophys. Res. Solid Earth 111, 1–4.
544 https://doi.org/10.1029/2005JB004010
545 Ortoleva, P., Merino, E., Moore, C., Chadam, J., 1987. Geochemical self-organization I: reaction-
546 transport feedbacks and modeling approach. Am. J. Sci.
547 https://doi.org/10.2475/ajs.287.10.979
548 Park, W.C., Schot, E.H., 1968. Stylolites: their nature and origin. J. Sediment. Res. 38, 175–191.
549 https://doi.org/10.1306/74D71910-2B21-11D7-8648000102C1865D
550 Passchier, C.W., Trouw, R.A.J., 2005. Microtectonics.
551 Peters, J.F., Muthuswamy, M., Wibowo, J., Tordesillas, A., 2005. Characterization of force chains
552 in granular material. Phys. Rev. E - Stat. Nonlinear, Soft Matter Phys. 72, 1–8.
553 https://doi.org/10.1103/PhysRevE.72.041307
554 Pluymakers, A.M.H., Spiers, C.J., 2015. Compaction creep of simulated anhydrite fault gouge by
555 pressure solution: Theory v. experiments and implications for fault sealing. Geol. Soc. Spec.

Publ. 409, 107–124. https://doi.org/10.1144/SP409.6

Renard, F., Bernard, D., Thibault, X., Boller, E., 2004. Synchrotron 3D microtomography of halite aggregates during experimental pressure solution creep and evolution of the permeability. Geophys. Res. Lett. 31, 1–4. https://doi.org/10.1029/2004GL019605

Renard, F., Dysthe, D., Feder, J., Bjorlykke, K., Jamtveit, B., 2001. Enchanced pressure solution creep rates induced by clay particles: Experimental evidence in salt aggregates. Geophys. Res. Lett. 28, 1295–1298. https://doi.org/10.1029/2000GL012394

Renard, F., Ortoleva, P., Gratier, J.P., 1997. Pressure solution in sandstones: influence of clays and dependence on temperature and stress. Tectonophysics 280, 257–266. https://doi.org/10.1016/S0040-1951(97)00039-5

Rutter, E.H., 1983. Pressure solution in nature, theory and experiment. J. Geol. Soc. London. 140, 725–740. https://doi.org/10.1144/gsjgs.140.5.0725

Rutter, E.H., Wanten, P.H., 2000. Experimental Study of the Compaction of Phyllosilicate-Bearing Sand at Elevated Temperature and with Controlled Pore Water Pressure. J. Sediment. Res. 70, 107–116. https://doi.org/10.1306/2DC40902-0E47-11D7-8643000102C1865D

Schindelin, J., Arganda-Carreras, I., Frise, E., Kaynig, V., Longair, M., Pietzsch, T., Preibisch, S., Rueden, C., Saalfeld, S., Schmid, B., Tinevez, J.-Y., White, D.J., Hartenstein, V., Eliceiri, K., Tomancak, P., Cardona, A., 2012. Fiji: an open-source platform for biological-image analysis. Nat. Methods 9, 676–682. https://doi.org/10.1038/nmeth.2019

Schutjens, P.M.T.M., Spiers, C.J., 1999. Intergranular pressure solution in NaCl: Grain-to-grain contact experiments under the optical microscope. Oil Gas Sci. Technol. 54, 729–750.

https://doi.org/10.2516/ogst:1999062

Spiers, C.J., Schutjens, P.M.T.M., Brzesowsky, R.H., Peach, C.J., Liezenberg, J.L., Zwart, H.J., 1990. Experimental determination of constitutive parameters governing creep of rocksalt by pressure solution. Geol. Soc. London, Spec. Publ. 54, 215–227. https://doi.org/10.1144/GSL.SP.1990.054.01.21

Sprunt, E.S., Nur, A., 1977. Destruction of porosity through pressure solution. Geophysics 42, 726–741.

Sprunt, E.S., Nur, A., 1976. Reduction of porosity by pressure solution: Experimental verification. Geology 4, 463–466.

Torabi, A., R.H., G., Fossen, H., Pingrose, P., Skurtveit, E., Ando', E., 2015. Strain localization in sandstone and its implications for CO2 storage. First Break 33, 81–92.

Tudisco, E., Andò, E., Cailletaud, R., Hall, S.A., 2017. TomoWarp2: A local digital volume correlation code. SoftwareX 6, 267–270. https://doi.org/10.1016/j.softx.2017.10.002

Van den Ende, M.P.A., Marketos, G., Niemeijer, A.R., Spiers, C.J., 2018. Investigating Compaction by Intergranular Pressure Solution Using the Discrete Element Method. J. Geophys. Res. Solid Earth. https://doi.org/10.1002/2017JB014440

Weyl, P.K., 1959. Pressure solution and the force of crystallization: a phenomenological theory. J. Geophys. Res. 64, 2001–2025. https://doi.org/10.1029/JZ064i011p02001

FIGURE CAPTIONS

Figure 1 a) Horizontal XY µCT slice and b) vertical XZ µCT slice of the NaCl-biotite sample, showing the different attenuation values of the materials: biotite in bright colour, NaCl grains in light grey and (brine-filled) pores in dark grey.

Figure 2 a) Compaction curves for the two samples (top). Roman numbers indicated the number of the 12 µCT dataset acquired: the reference scan is not numbered (see section 3.2). b) Evolution of bulk strain rates with increasing deformation for the two samples, in log-log scale.

Figure 3 Vertical µCT slices of four different shortened datasets, for pure NaCl (left column) and NaCl-biotite samples (right column), respectively. Roman numbering refers to Figure 2a. White arrows indicate areas of reduced porosity, where NaCl grains indent more, losing their cubic habit, and/or precipitation sites.

Figure 4 a) Evolution of the pore volume (in μm^3) in the two sample compositions for increasing compaction time (hours). The percentages inside the bars indicate the porosity, calculated through the *Volume Fraction* operator from the 400^3 voxels subvolumes (see section 2.2.4). Initial porosity fraction (ϕ_0), calculated from the undeformed 400^3 voxels subvolumes, is given in the legend for the two samples. Errors bars obtained through erosion and dilation of original segmented pore space. b, c, d) Temporal evolution (in hours, 'hs') of porosity slice by slice ("Porosity 2D") as a function of the vertical Z axis for the two samples.

Figure 5 Relative shortening of the biotite-bearing and NaCl-bearing layers. The grey shaded area indicates the time interval over which pore connectivity breaks down within the NaCl-biotite layer (see section 3.2.2).

Figure 6 Interconnectivity of the pore space as a function of deformation for the two samples. Different colours indicate disconnected pore clusters.

Figure 7 DVC results for the NaCl sample, for increasing compaction time (indicated in hours, '*hs*') and vertical shortening (in percentage). Images are obtained as vertical slices through the

middle of the sample. For a better comparison, maximum shear strain (*Shear Strain*) and volumetric strain (*Volum. Strain*) results are reported together with the pair of *x-ray μCT* images used for the correlation for each interval time. Black areas identify locations where the correlation failed. Higher values of maximum shear strain are represented in the images by warmer colours, while negative values of volumetric strain (indicating compaction) are represented by blue colours (white circles). Note the relatively homogeneous distribution of shear strains, with local highs.

Figure 8 DVC results for the NaCl-biotite sample, for increasing compaction time (indicated in hours, '*hs*') and vertical shortening (in percentage). Images are obtained as vertical slices through the middle of the sample. For a better comparison, maximum shear strain (*Shear Strain*) and volumetric strain (*Volum. Strain*) results are reported together with the pair of *x-ray μCT* images used for the correlation for each interval time. Black areas identify locations where the correlation failed. Higher values of maximum shear strain are represented in the images by warmer colours, while negative values of volumetric strain (indicating compaction) are represented by blue colours (white circles). Note the extreme intense values in areas where the biotite flakes are located (high shear strains, negative volumetric strains).

Figure 9 The images show the distributions of local strain rates (in s-1), calculated from DVC results, for both samples: a) maximum shear strain rates, b) volumetric strain rates. To obtain the strain rates, the strain values, obtained from the DVC results, are divided by the time interval between each pair of correlations. Black areas identify locations where the correlation failed.

643 **Figure 10** SEM images of recovered samples: a) triple junction (highlighted by white arrows)
644 between grains in the pure NaCl sample; b) close up from the red square in a, note the suture
645 zone (white arrows) between NaCl grains; c, d) NaCl grains indenting biotite flakes (Bt) in the
646 NaCl-biotite sample.

647

Figure1
Click here to download high resolution image

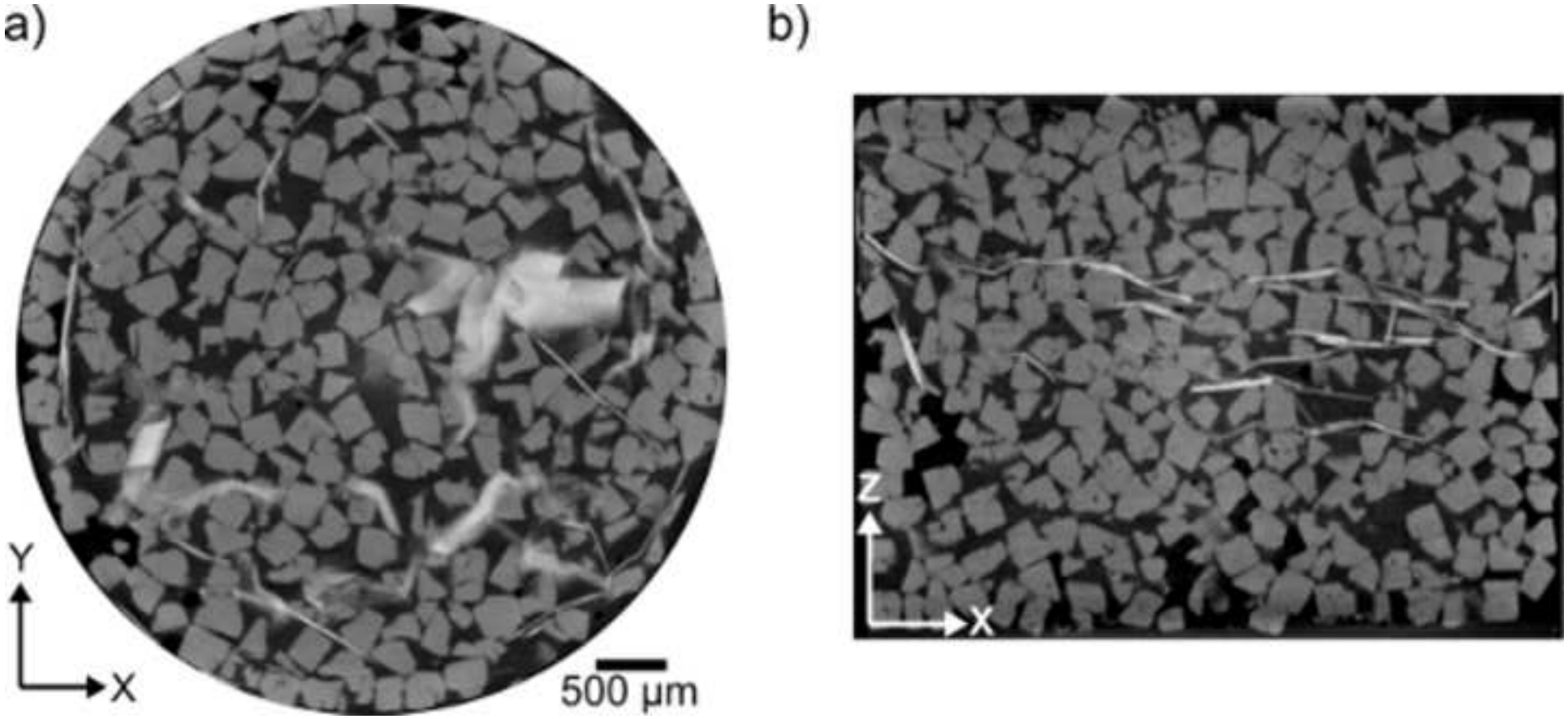

Figure2

Click here to download Figure: Figure2.pdf

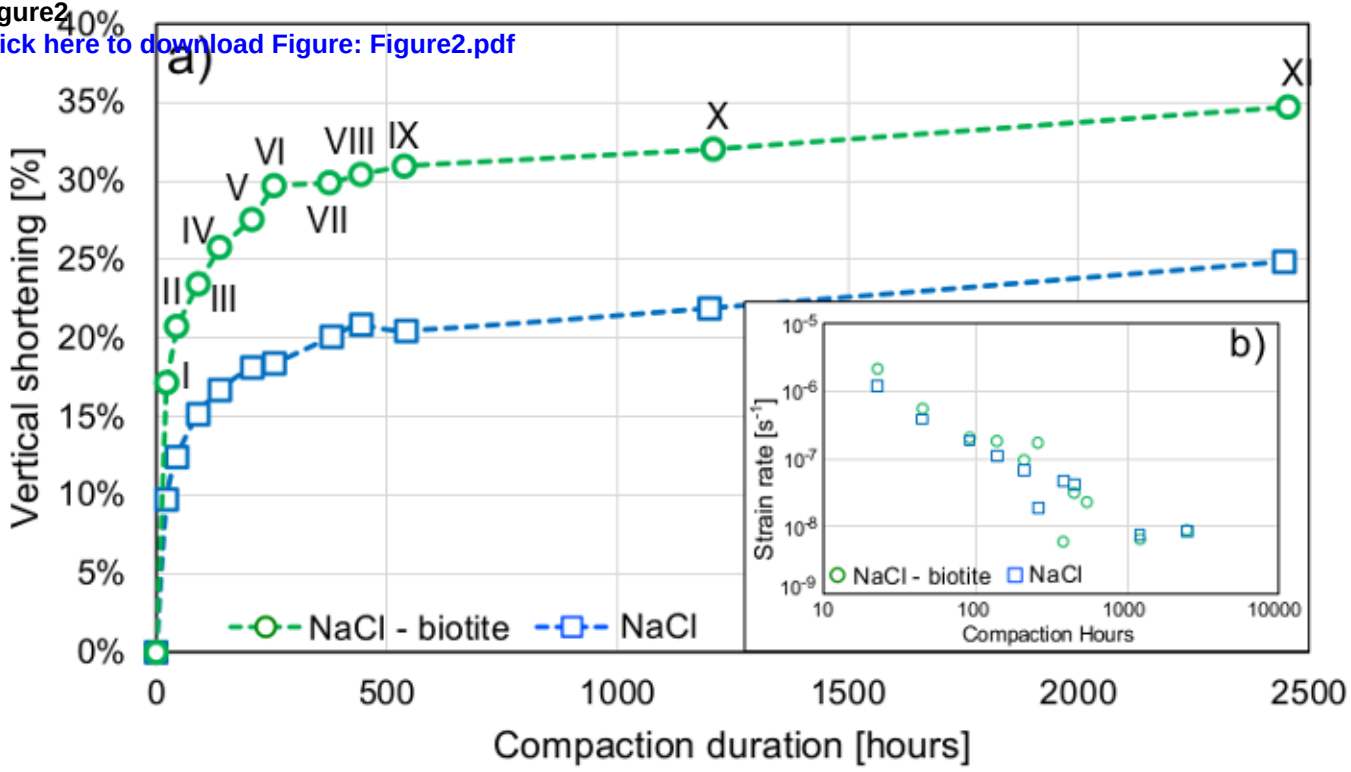

Figure3
Click here to download high resolution image

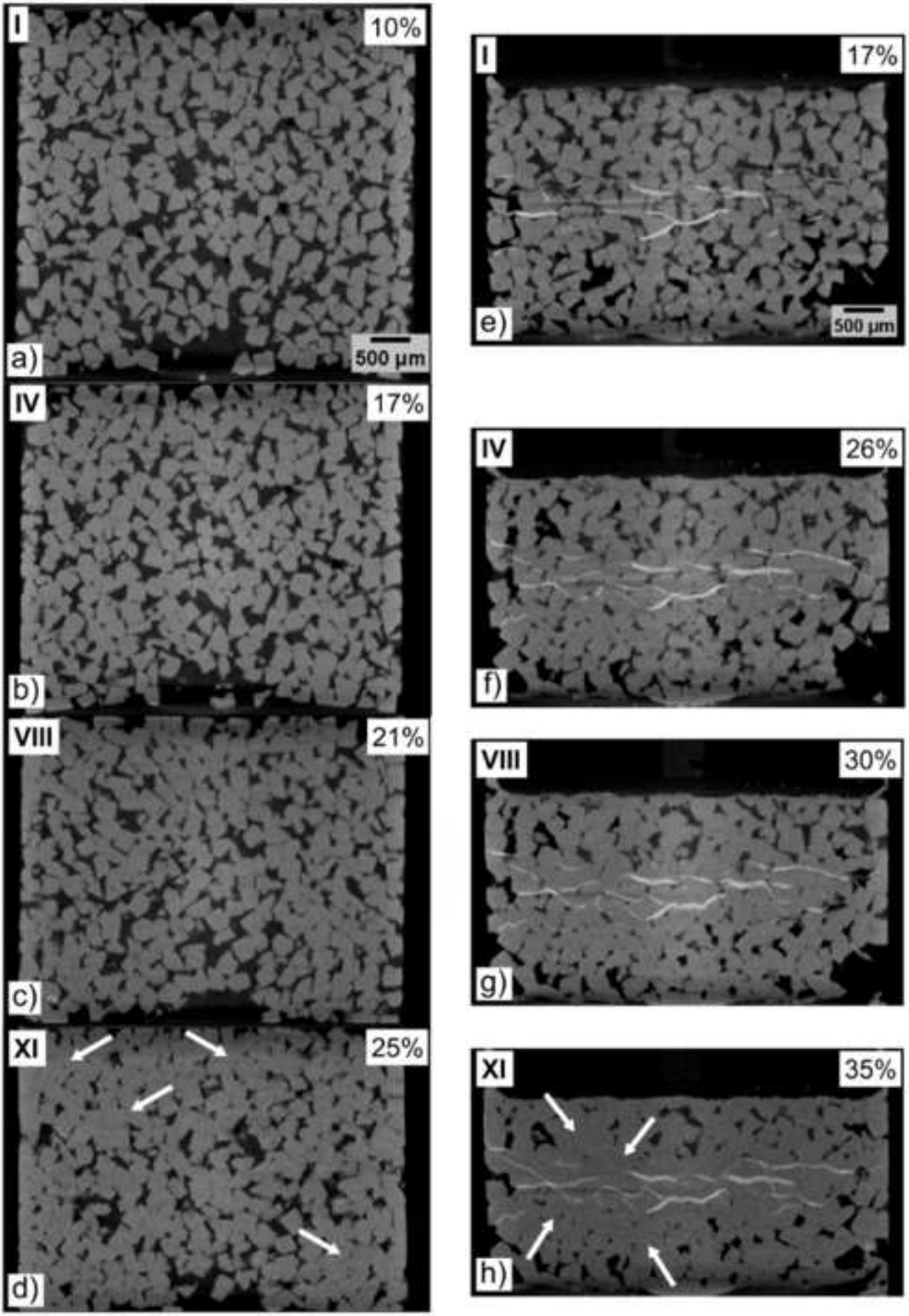

Figure4

Click here to download high resolution image

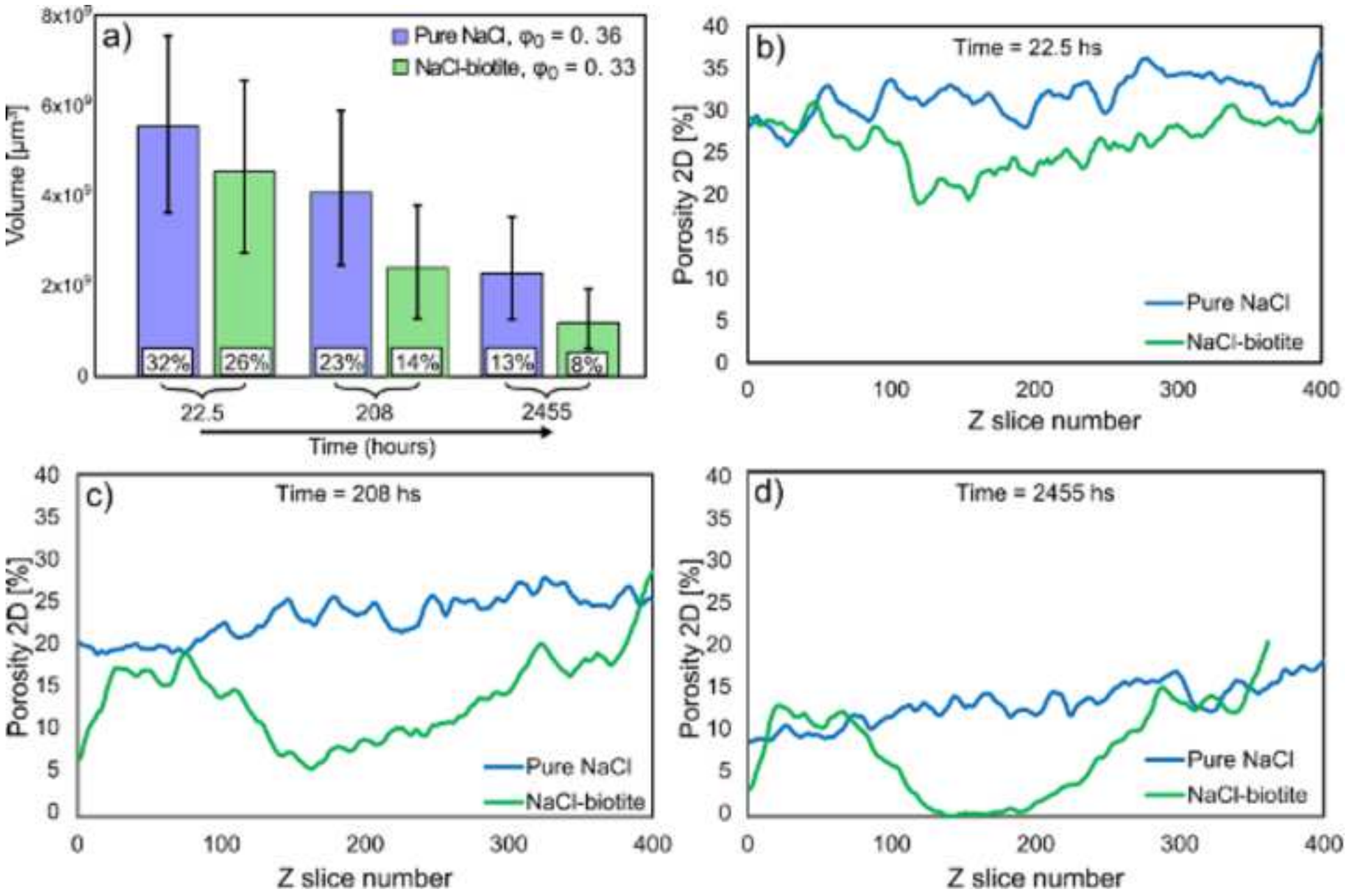

Figure5

Click here to download Figure: Figure5.pdf

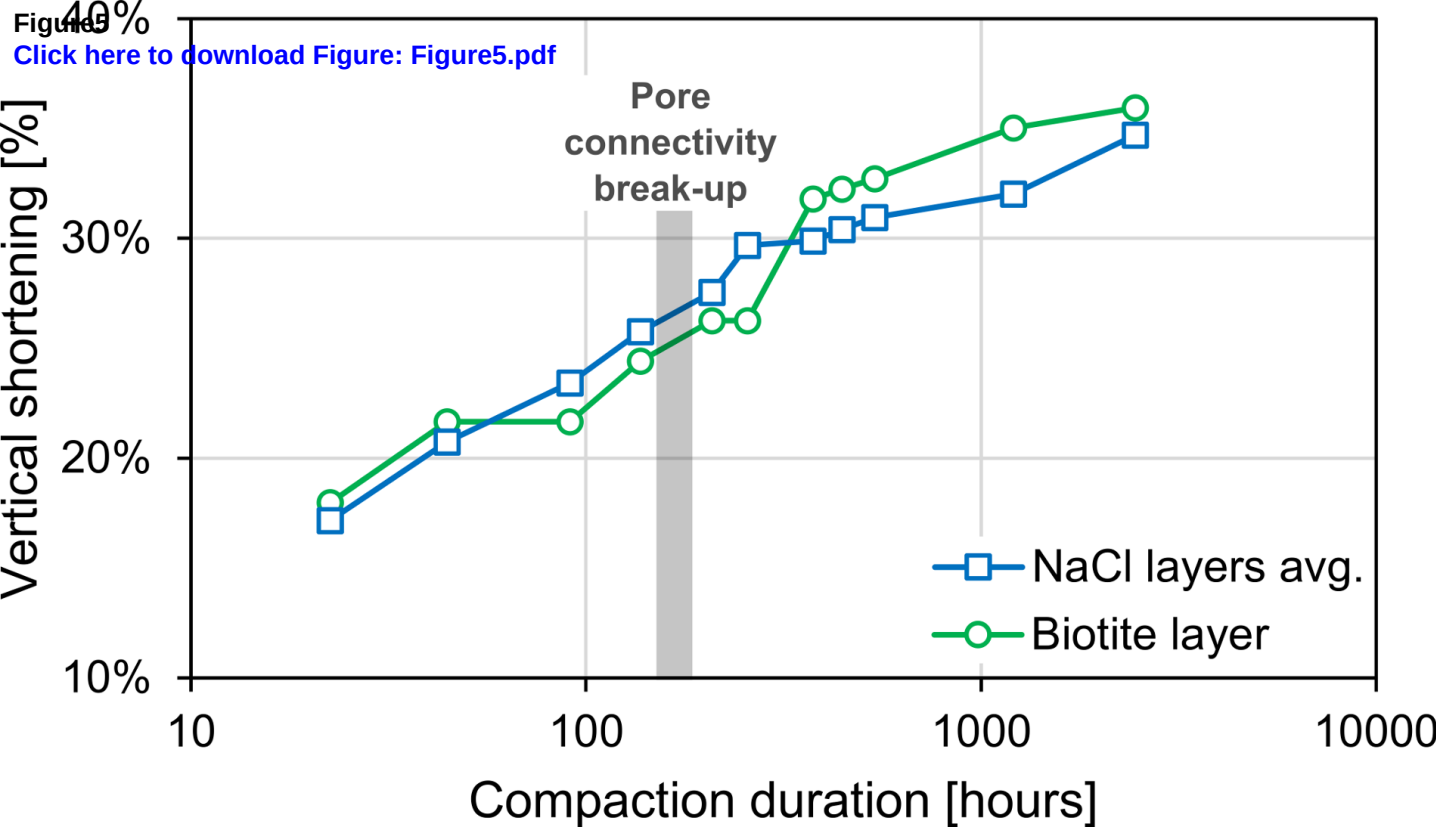

Figure6

Click here to download high resolution image

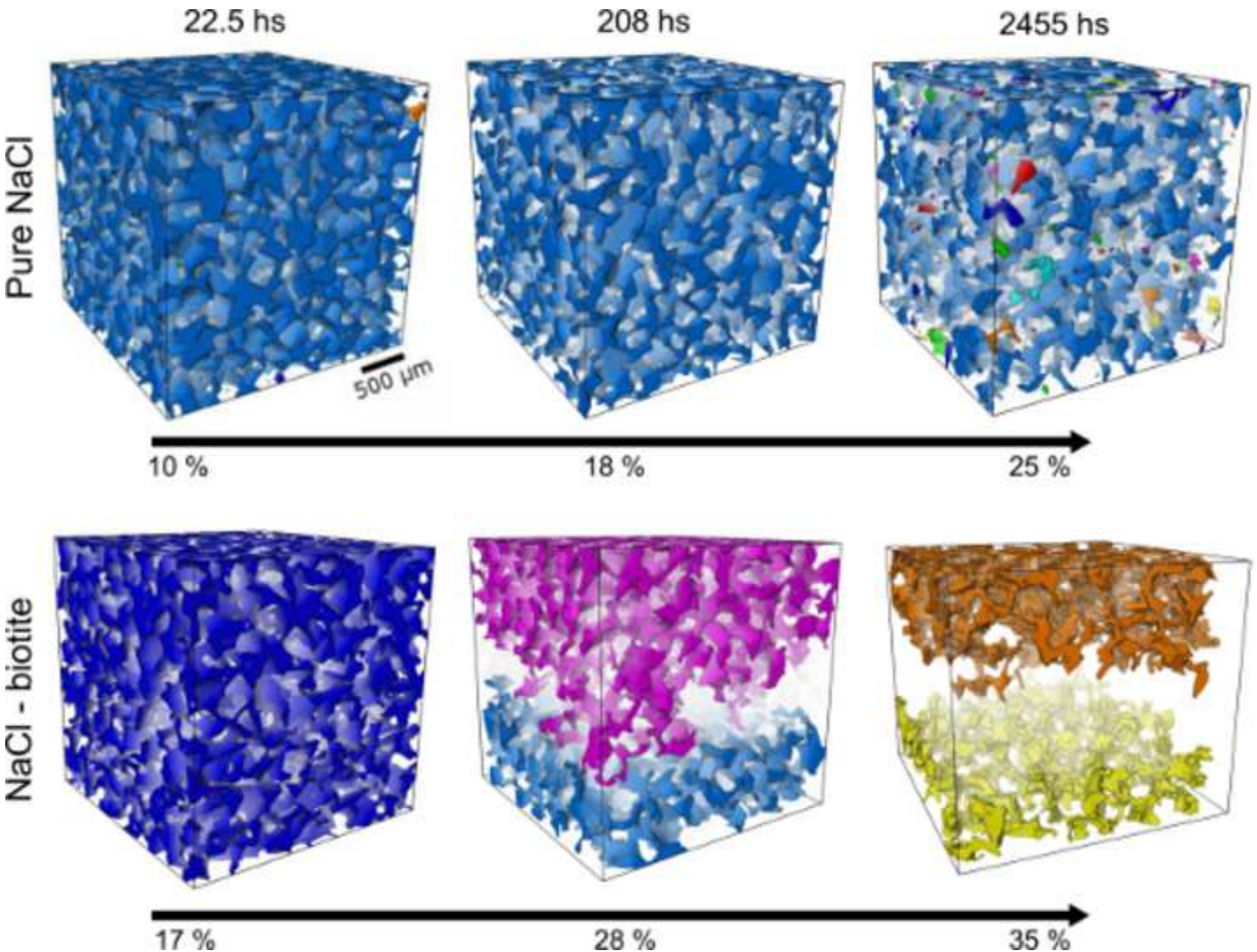

Figure7

Click here to download high resolution image

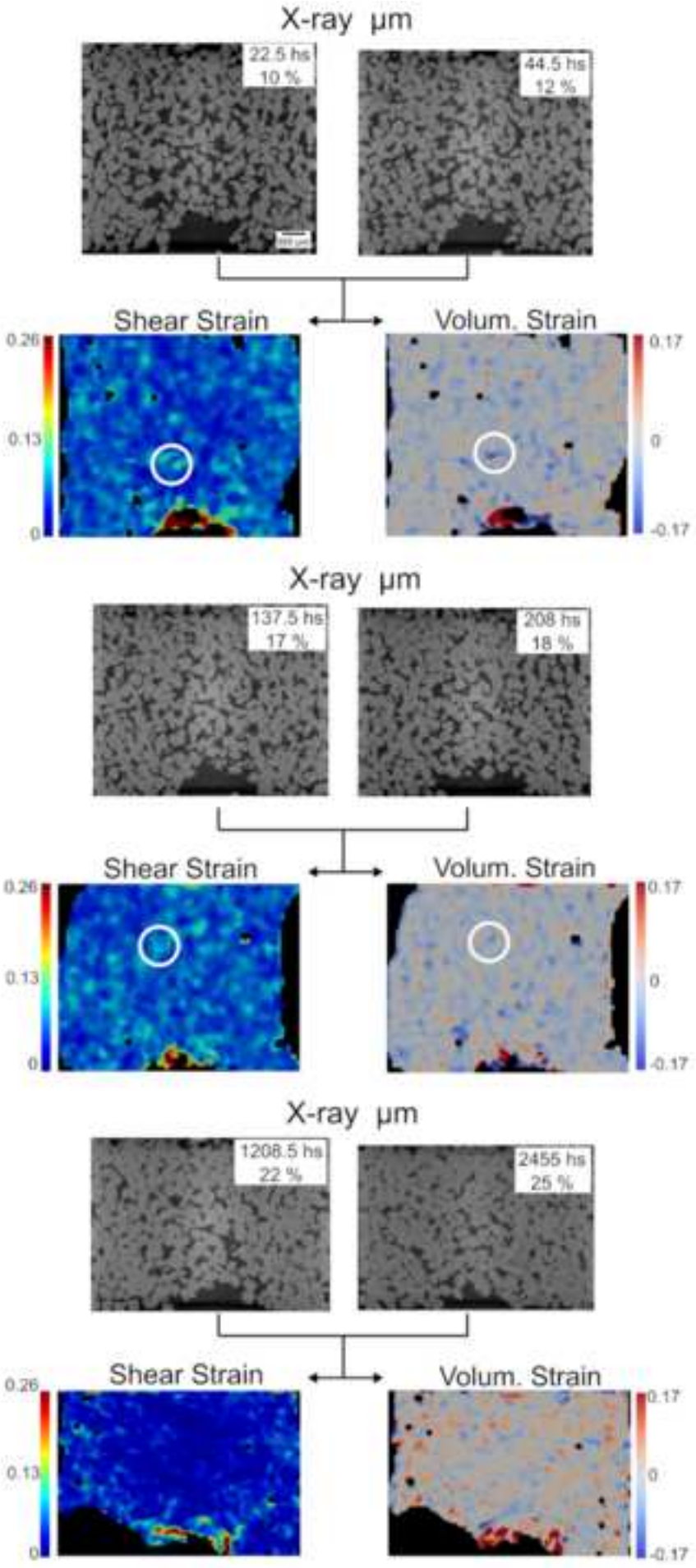

Figure8

Click here to download high resolution image

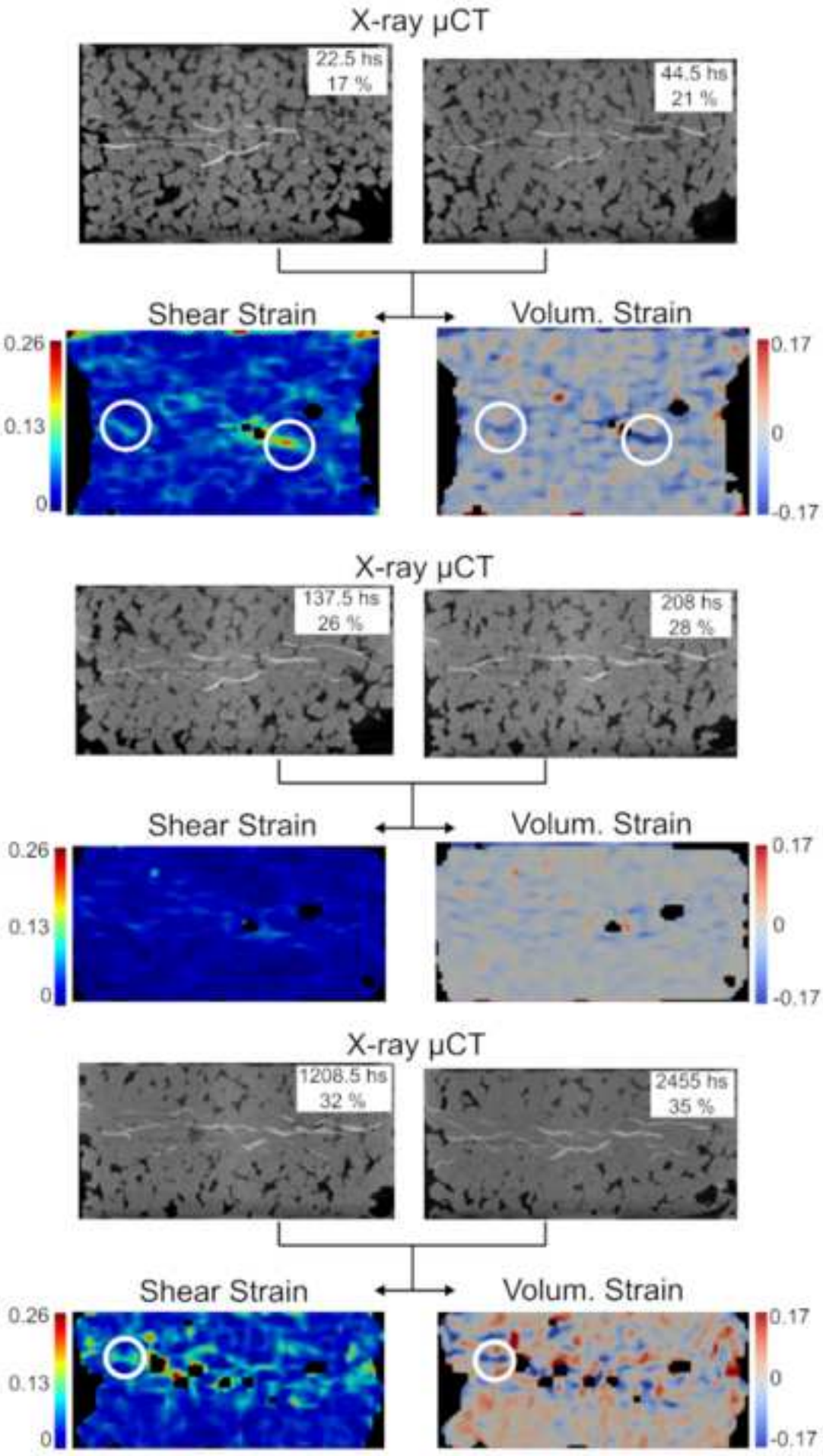

Figure9

Click here to download high resolution image

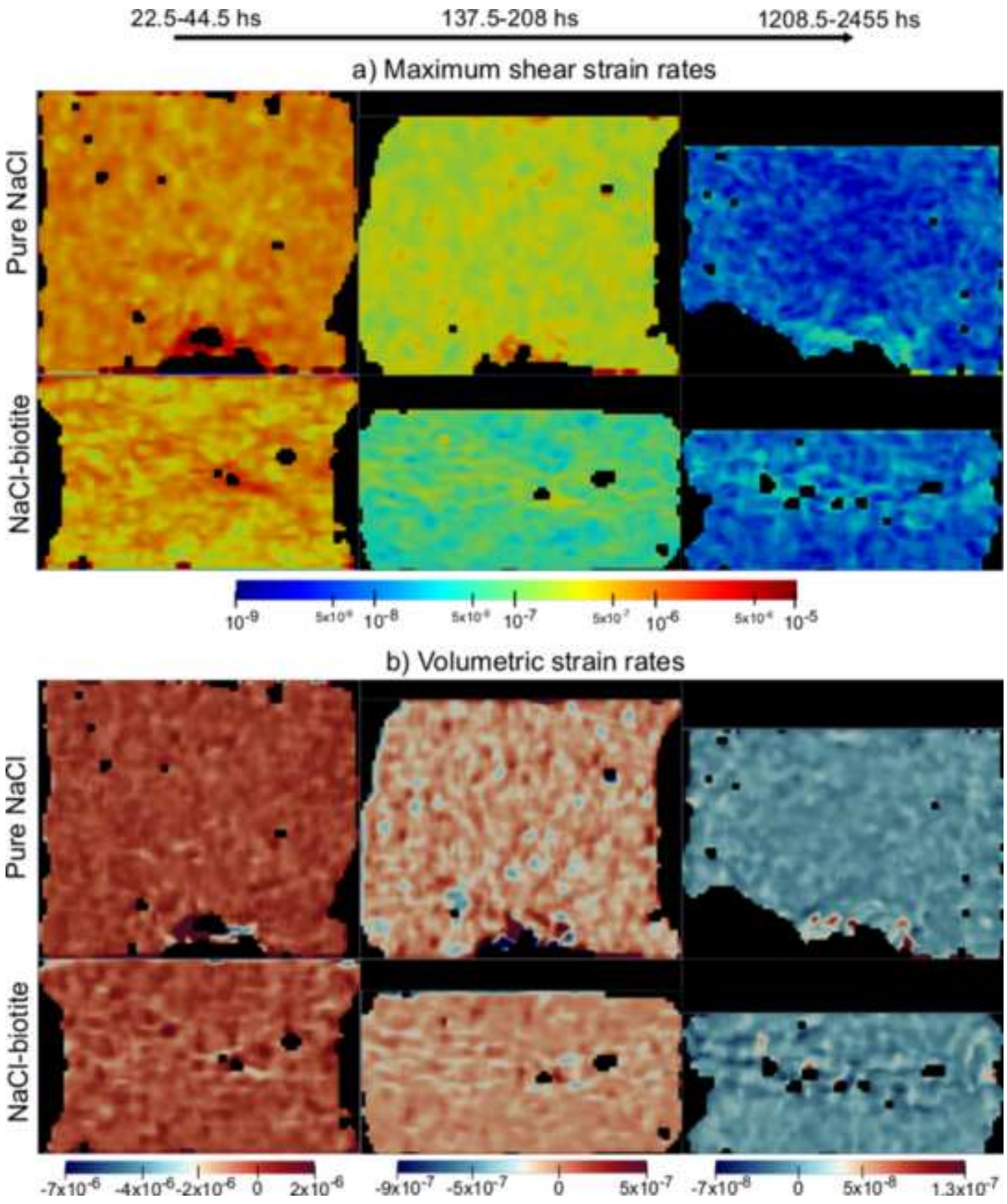

Figure10

Click here to download high resolution image

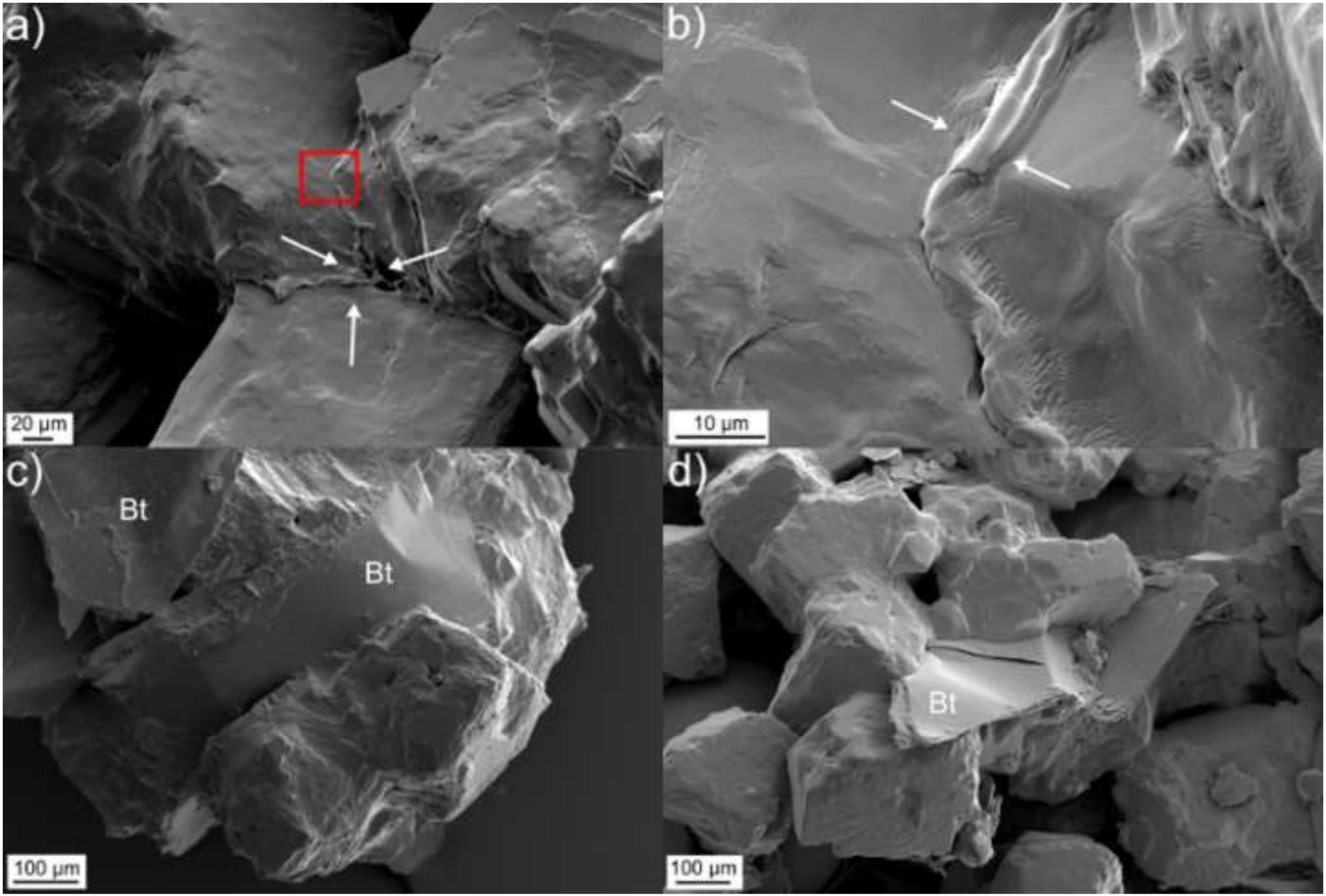

Figure 7(high-resolution)

Click here to download Figure (high-resolution): Figure7(high-resolution).tif

Figure 8(high-resolution)

Click here to download Figure (high-resolution): Figure8(high-resolution).tif

Figure 1(high-resolution)

Click here to download Figure (high-resolution): Figure1(high-resolution).tif

Figure 2(high-resolution)

Click here to download Figure (high-resolution): Figure2(high-resolution).pdf

Figure 3(high-resolution)

Click here to download Figure (high-resolution): Figure3(high-resolution).tif

Figure 4(high-resolution)

Click here to download Figure (high-resolution): Figure4(high-resolution).tif

Figure 5(high-resolution)

Click here to download Figure (high-resolution): Figure5(high-resolution).pdf

Figure 6(high-resolution)

Click here to download Figure (high-resolution): Figure6(high-resolution).tif

Figure 9(high-resolution)

Click here to download Figure (high-resolution): Figure9(high-resolution).tif

Figure 10(high-resolution)

Click here to download Figure (high-resolution): Figure10(high-resolution).tif

Supplementary material for online publication only

Click here to download Supplementary material for online publication only: Macente2018_EPSL_SI_revised.docx

Supplementary material GIF

Click here to download Supplementary material (video): Gif1.gif

Supplementary material GIF

Click here to download Supplementary material (video): Gif2.gif